nature communications

Article

https://doi.org/10.1038/s41467-025-59385-y

Stability of the fcc phase in shocked nickel up to 332 GPa

Received: 27 December 2024

Accepted: 22 April 2025

Published online: 12 May 2025

Check for updates

Kimberly A. Pereira[1], Samantha M. Clarke[2] ✉, Saransh Singh[2], Richard Briggs[2], Christopher P. McGuire[2], Hae Ja Lee[3], Dimitri Khaghani[3], Bob Nagler[3], Eric Galtier[3], Eric Cunningham[3], David McGonegle[4,5], Sally J. Tracy[6], Cara Vennari[2], Martin G. Gorman[7], Amy L. Coleman[2], Carol Davis[2], Trevor Hutchinson[2], Jon H. Eggert[2], Raymond F. Smith[2] & James P. S. Walsh[1] ✉

Despite making up 5-20 wt.% of Earth's predominantly iron core, the melting properties of elemental nickel at core conditions remain poorly understood, due largely to a dearth of experimental data. We present here an in situ X-ray diffraction study performed on laser shock-compressed samples of bulk nickel, reaching pressures up to ~ 500 GPa. Hugoniot states of nickel were targeted using a flat-top laser drive, with in situ X-ray diffraction data collected using the Linac Coherent Light Source. Rietveld methods were used to determine the densities of the shocked states from the measured diffraction data, while peak pressures were determined using a combination of measured particle velocities, shock transit times, hydrodynamic simulations, and laser intensity calibrations. We observed solid compressed face-centered cubic (fcc) Ni up to at least 332 ± 30 GPa along the Hugoniot—significantly higher than expected from the majority of melt lines that have been proposed for nickel. We also bracket the partial melting onset to between 377 ± 38 GPa and 486 ± 35 GPa.

Nickel is an abundant impurity element in the Earth's iron-rich core and likely also plays a significant role in other planetary interiors containing metallic cores[1,2]. In the case of the Earth, estimates from cosmochemistry suggest nickel could compose between 5 and 20 w.t.% of the core[3–5]. It has long been recognized that a solid inner core is currently crystallizing out of the core liquid[6]. The density contrast between solid and liquid and the depth of the inner core boundary are well constrained by seismology, but the composition and melting temperature of the core material at the extreme conditions of the inner core (330 GPa to 360 GPa) remain unknown. The melting temperature is particularly unconstrained and could change by up to 1000 K depending on the impurity elements alloyed with iron, and with the experimental platform used to infer melting.

Recent interpretations of seismic data have revealed a previously unknown complexity in the structure of the inner core[7,8]. This signature may be crystallographic in origin, and thus explained by an "innermost core," or it could be indicative of trapped liquid along grain boundaries of the inner core solid[9,10]. While many studies have investigated iron and iron alloys under planetary core conditions[11–29], direct observations of the structure and phase of relevant impurity end-members, such as nickel, are lacking. The stability of high-pressure phases, and in particular the melting transition and co-existing solid structure, are essential inputs for thermodynamic mixing models of core-relevant compositions[30]. This is especially true for nickel, which mixes on the liquidus with iron in the face-centered cubic (fcc) phase at pressures below 100 GPa[31,32]. At the higher pressures relevant to the

[1]Department of Chemistry, University of Massachusetts Amherst, Amherst, MA, USA. [2]Lawrence Livermore National Laboratory, Livermore, CA, USA. [3]Linac Coherent Light Source, SLAC National Accelerator Laboratory, Menlo Park, CA, USA. [4]Department of Physics, Clarendon Laboratory, University of Oxford, Oxford, UK. [5]Atomic Weapons Establishment, Aldermaston, UK. [6]Earth and Planets Laboratory, Carnegie Institution for Science, Washington, DC, USA. [7]First Light Fusion, Oxford, UK. ✉e-mail: clarke30@llnl.gov; jpswalsh@umass.edu

core, the liquidus phase of nickel has not yet been observed experimentally. There are some predictions that a body-centered cubic (bcc) polymorph of nickel may be stabilized at high pressures and temperatures, which could change the mixing properties between iron and nickel[33–35], while recent ab initio calculations suggest that alloying of nickel affects the crystallization sequence of iron solid phases at core pressures[35].

Although extensive shock studies were performed on nickel starting in the 1950s, no information regarding the onset of melt can be extracted from those measurements[36–45]. Given this lack of melting data on nickel, many geophysical models[46,47] have instead relied on direct measurements of iron at core conditions, and on extrapolations from lower-pressure measurements on nickel and iron-nickel alloys[11–18,29]. Despite the existence of a large body of theoretical work performed on nickel under extreme pressures and temperatures, to date there have been very few experimental studies into the crystal structure of nickel at core conditions[48]. This lack of a direct experimental examination of the crystal structure of nickel along the principal Hugoniot at core-relevant pressures means that the melt line of nickel remains weakly constrained above 100 GPa[49,50]. A measurement of the incipient melting and melt-completion pressures—along with the co-existing solid crystal structure—would provide the first experimental inputs for mixing models of iron and nickel phase relations.

Recent advances using in situ X-ray diffraction (XRD) methods for the study of matter under dynamically-loaded stresses provide unprecedented experimental access to atomic structure and bonding under extreme conditions[51–58], and have been used to redefine the melting curves of elements such as molybdenum, tantalum, and iron by measuring the pressure at which solid and liquid co-exist on shock compression[59–61]. In these cases, the slope of the melting curve has been found to be much steeper than previously determined in the ~100 GPa to ~200 GPa range accessible to static compression, demonstrating the importance of collecting data in the multi-Mbar range.

Here, we present an in situ XRD study on shocked bulk nickel, allowing us to measure the onset of melt. We find that solid single-phase fcc-Ni persists to higher pressures along the principal Hugoniot than would be expected from the majority of proposed melt lines, and arrive at a minimum incipient melting pressure of 332 ± 30 GPa.

Results and discussion

Visual inspection of the VISAR images reveals that the breakout was planar over the region probed by the X-rays in all of the runs reported here. A summary of the VISAR data is shown in Table 1. We were able to determine breakout times for all runs, but particle velocities and associated pressures could only be determined for runs 097, 099, and 493. At laser intensities of 1.56×10^{13} W cm^{-2} and higher, we observed a blanking of our VISAR data that was likely due to the LiF window becoming opaque at elevated pressures—a phenomenon that is known to occur at pressures above ~200 GPa in LiF (corresponding to pressures above ~400 GPa in Ni)[62,63]. For this reason, particle velocities at the Ni–LiF interface could not be experimentally determined for runs 160, 151, 420, 422, and 149.

To determine the peak stress in the sample for runs 097 and 099, we impedance-matched the particle velocity at the Ni–LiF interface, yielding stresses of 183 ± 23 GPa and 240 ± 18 GPa for runs 097 and 099, respectively[64]. These data are displayed in Table 1. Other data from the VISAR measurements, including the time the shockwave reached the Ni–LiF interface (breakout time), as well as the time the X-ray probe was triggered (probe time), are presented in Table 1. From these data, we are confident that our X-ray diffraction data were obtained under compression.

To determine pressure for runs 160, 151, 420, and 422, we used the densities determined from fitting the X-ray diffraction data to calculate pressures based on a fit to the literature data[36–38,41–44,65]. To determine a pressure for Run 149, where solid fcc-Ni was not observed, the pressures determined from diffraction were used to construct a calibration curve fitted against laser intensities. To calculate laser intensity values, we used measurements of the actual laser spot profile, which gave a more accurate measure of the laser spot diameter and intensity profile than the nominal values. These measurements showed that 50% of the laser energy is contained within 139.7 µm for the 150 µm phase plates, and within 240.8 µm for the 300 µm phase plates. When calculating laser intensity, this 50% factor was included, and the measured diameters were used to calculate the intensities. Pressures derived from both methods are presented in Table 2. Comparing Tables 1 and 2, we see excellent agreement between the pressures derived from VISAR measurements and the pressures derived from XRD-measured densities. The supplementary material contains a comparison table showcasing good agreeement between pressures determined from VISAR, pressures derived from XRD densities, and pressures calculated from the laser intensity calibration curve.

In the following sections, stresses are reported with experimental errors for those shots where VISAR analysis was possible (runs 097, 099, and 493); for all other shots we report pressure values determined either directly from densities matched to a fit to literature data (runs 160, 151, 420, and 422), or using our laser intensity calibration curve (run 149). For the determination of the pressures derived from the X-ray diffraction measured density, we constructed an exponential fit to literature pressure–density data. The error is a combination of (1) the Rietveld refinement model of the XRD, with the error calculated out to 3σ, and (2) a 99% confidence interval of the exponential fit to the literature data. For the determination of pressures from the laser intensity calibration curve, the error arises from a 99% confidence interval to Equation (3).

Table 1 | Summary of VISAR data for each run

Run ID	Percent compressed[a]	Expected transit time through Ni foil (ns)	VISAR 1 Breakout Time (ns)	VISAR 2 breakout Time (ns)	Probe time (ns)	Particle velocity (km s^{-1})	Stress (GPa)
097	83.0%	2.90	12.5 ± 0.1	12.4 ± 0.1	12	3.6 ± 0.4	183 ± 23
099	93.4%	2.63	10.9 ± 0.1	11.2 ± 0.1	11	4.2 ± 0.2	240 ± 18
160	67.0%	2.36	10.6 ± 0.1	10.6 ± 0.1	9.5	—	—
151	86.8%	2.17	9.4 ± 0.1	9.4 ± 0.1	9	—	—
420	62.8%	2.10	10.3 ± 0.1	10.4 ± 0.1	10.2	—	—
422	69.8%	2.08	10.5 ± 0.1	10.5 ± 0.1	10.4	—	—
149	93.8%	2.06	9.4 ± 0.1	9.7 ± 0.1	9	—	—
493	85.5%	1.16	4.3 ± 0.1	4.5 ± 0.1	4	5.2 ± 0.3	332 ± 30

[a]Determined by comparing the integral of the (111) peak in the preshot and shot X-ray diffraction images.

https://doi.org/10.1038/s41467-025-59385-y

Table 2 | Summary of key parameters determined from each run

Run ID	Laser intensity (W cm^{-2})	Observed phases	Compressed *a* axis (fcc-Ni)	Density (g cm^{-3})	Pressure (GPa)
097	5.05×10^{12}	fcc	3.1307 (5)	12.72 (5)	192 ± 20[a]
099	7.37×10^{12}	fcc	3.0729 (2)	13.44 (1)	274 ± 19[a]
160	1.69×10^{13}	fcc	3.017 (5)	14.2 (1)	377 ± 38[a]
151	1.82×10^{13}	fcc + liquid	2.966 (1)	14.92 (2)	486 ± 35[a]
420	2.22×10^{13}	fcc + liquid	2.953 (4)	15.1 (2)	515 ± 67[a]
422	2.23×10^{13}	fcc + liquid	2.947 (5)	15.2 (1)	531 ± 52[a]
149	2.28×10^{13}	liquid	—	—	527 ± 87[b]
493	1.50×10^{13}	fcc	3.034 (2)	13.97 (7)	344 ± 31[a]

[a]Determined using a fit to literature data[36–38,41–44,65].
[b]Determined using laser intensity calibration curve.

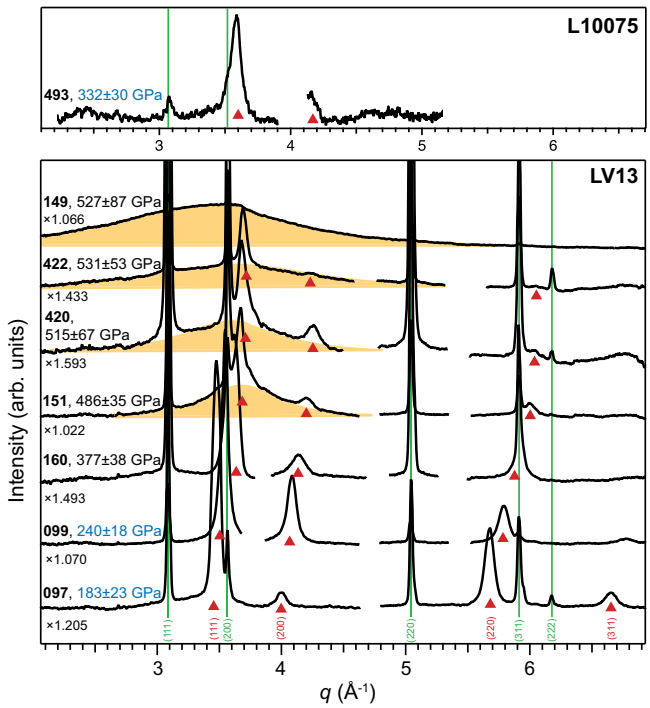

Fig. 1 | Waterfall plot of the integrated X-ray intensities vs. *q* of the seven reported runs from LV13 (bottom) and one reported run from L10075 (top). Fitted polynomial backgrounds have been subtracted for clarity (see Supplementary Materials for uncorrected integrations, Figs. S3–S9). Ambient fcc-Ni reflections are highlighted with green bars. Locations of Bragg reflections from the compressed fcc-Ni, where present, are highlighted with red triangles to provide a guide to the eye. Diffraction patterns are ordered in ascending pressure from bottom to top (see Table 2). Shaded orange areas show a single Gaussian peak, which was fitted along with a polynomial background (subtracted here), and are taken to indicate a diffuse signal arising from the presence of melt. Pressures in blue represent pressures calculated from VISAR data, whereas pressures in black indicate pressures calculated from densities modeled by Rietveld refinements of the XRD data or pressures from the laser intensity calibration curve.

Figure 1 shows the integrated diffraction intensities plotted in *q*-space for the selected runs. The main panel features seven runs from the primary experiment being reported here (LV13), arranged with the incident laser energy upon the target increasing from bottom to top. A separate panel is used to plot a single run from a second experiment (L10075), which is discussed below. The reflections from uncompressed fcc-Ni are clearly observed in all runs, consistent with the X-rays having arrived prior to shock breakout at the Ni–LiF interface. Reflections that can be assigned to compressed fcc-Ni are highlighted with red triangles, and their positions were fit simultaneously with whole-pattern Rietveld methods using the GSAS-II package[66] to determine the density of the compressed phase. Density values and results from the GSAS-II package[66] fits are shown in Table 2. The *d*-spacing of the individual peaks of the compressed phase was also determined with single-peak fitting and compared with the d-spacing expected for fcc-Ni from the literature (Supplementary Materials)[36–38,41–44,65]. The close agreement with the expected spacing confirms a lack of significant distortion away from cubic symmetry.

For the compressed (111) reflection, we see a clear shift to higher *q* with increasing shock energy. In run 097, it appears at slightly lower *q* than the ambient (200) reflection; in runs 099 and 160, it overlaps with the ambient (200) reflection; in runs 151, 420, and 422, it separates from the ambient (200) reflection and continues to move to higher *q*. We also observe the emergence of a broad diffuse signal centered on the compressed (111) peak in runs 151, 420, 422, and 149 (vida infra).

In all runs, the texture of the diffraction (azimuthal intensity around Debye-Scherrer cones, see Supplementary Materials) from the ambient samples is similar, showing distinct intensity variations along the azimuth that are typical of rolled foils. However, during shock, the Bragg intensity of the compressed (200) reflection becomes much more textured, and in all cases, the majority of the intensity arises from a single localized Bragg spot. This is clearly seen in the dewarped images plotted in the Supplementary Materials. This change in texture is evidence of a significant reorganization of crystalline domains, consistent with a large uniaxial compression of the sample[59].

We examined the measured XRD images for signs of diffuse scattering that may provide evidence of liquid, as has been well-documented in studies on other materials[14,67–76]. During the ambient pressure melting of nickel, a diffuse signal arising from ambient liquid nickel appears at a *q*-spacing of ~3.1 Å^{-1}, closely matching the position of the (111) Bragg peak[77,78]. We can thus expect the *q*-spacing of nickel melt signal under high pressures to be close to the (111) Bragg peak position at that density. The XRD runs can be separated into those which show no obvious diffuse scattering above the background (097 and 099), and those in which a distinct broad peak has appeared alongside the compressed fcc-Ni peaks, and whose position can be refined during Rietveld modeling using a Gaussian peak on top of the polynomial background (151, 420, 422, and 149). We extracted the fitted position of each of these peaks and found that they fall within the range 3.5 Å^{-1} to 3.7 Å^{-1}, which is consistent with diffuse signal from a dense nickel liquid (i.e., melt). (For a discussion of the minimum melt detectability, see the Supplementary Materials.)

We compared our shock compression data to literature data on nickel in order to assess the consistency between our results and the field as a whole[36–38,41–44,65]. Figure 2 shows a pressure–density plot with our measured density values placed on a Hugoniot calculated from the literature data[36–38,41–44,65]. For the LV13 dataset, the data points are color-coded to distinguish whether or not the pressure comes from the Rietveld refined density (green), from VISAR measurements (purple), or from the laser intensity calibration curve (red). Similarly, data from the L10075 dataset are color-coded to identify whether the pressure came from the Rietveld refined density (open purple) or from VISAR measurements (teal). We also plot literature data as well as recent computational Hugoniot data, and find our data to be consistent.

The melt curve of nickel as a function of pressure and temperature has been experimentally studied in static compression experiments up to pressures of ~100 GPa, while ab initio techniques have been used to calculate the melt curve up to ~330 GPa. Perhaps somewhat surprisingly, the slope of the melt curve at higher pressures varies quite dramatically between studies (see Fig. 3)[33,50,67,68,70,79–91].

https://doi.org/10.1038/s41467-025-59385-y

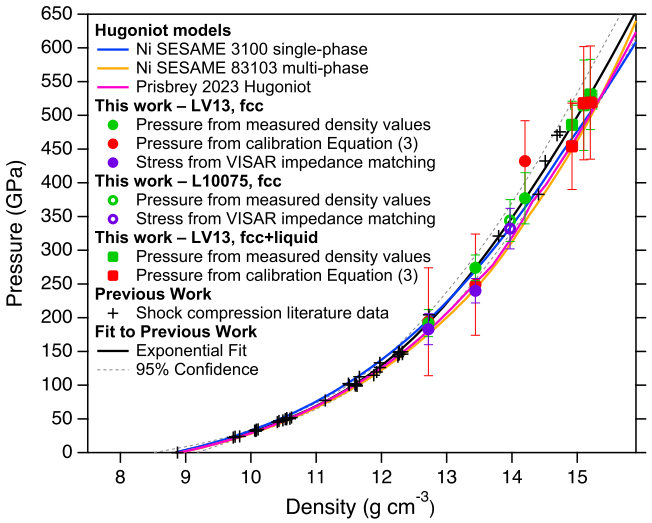

Fig. 2 | Data obtained from this work plotted alongside shock compression literature data and Hugoniot data. Three methods to obtain the peak pressure for each run, detailed in the Supplementary Materials, are represented for the LV13 campaign. Pressure values calculated from the measured density values obtained from the X-ray diffraction images are plotted as green points. Pressure values determined from the calibration equation described by Equation (3) are plotted as red points. Pressure values for runs 097 and 099 were found by VISAR impedance matching and are plotted as purple points (note that VISAR data for the other runs is not available due to the high opacity of the LiF window at high pressures). For the L10075 campaign, pressure from the measured density values is represented as open green points, whereas pressure from VISAR measurements is shown as open purple points. Circles represent runs where fcc-Ni was observed, whereas squares represent runs where fcc-Ni and liquid were observed. Data from the shock compression literature is shown as black crosses[36–38,41–44,65]. An exponential fit to the literature data is represented as a black line, with 95% confidence intervals shown as gray dashed lines. This exponential fit included data up to 1000 GPa, which is not pictured above. Three Hugoniot models are also shown. In orange is the Ni SESAME 83103 multi-phase Hugoniot, in blue is the Ni SESAME 3100 single-plase Hugoniot, and in pink is the Ni Hugoniot by Prisbrey[92–94].

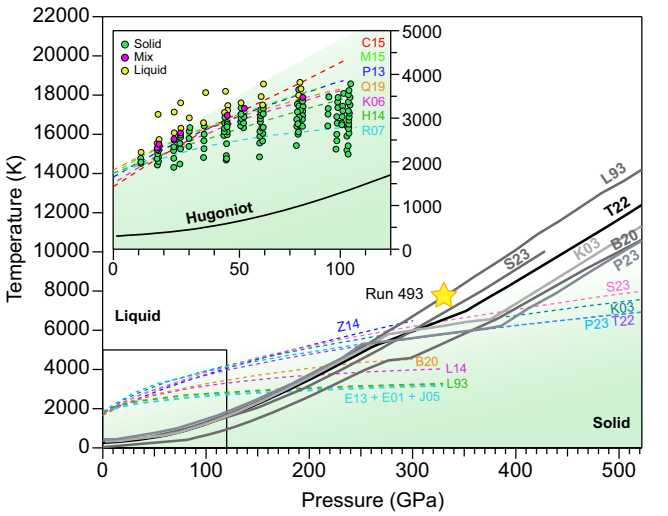

Fig. 3 | Temperature–pressure phase diagram of nickel illustrating the large spread of reported melt lines. The inset shows theoretical melt lines proposed for low pressures, all of which terminate at 100 GPa. All melt lines are plotted as dashed lines. Identifying codes are a combination of first-author surname initial and year of publication, and are tabulated in full in the Supplementary Materials. Data points shown in the inset are taken from the static compression melting experiments reported in ref. 70 and are color coded to indicate whether the authors observed solid Ni, liquid Ni, or a mix of the two (see legend). The main plot shows the reported melt lines that extend beyond 100 GPa. In the main plot, the single-phase SESAME 3100 Ni Hugoniot, the multi-phase SESAME 83103 Ni Hugoniot, and several other Hugoniot models from the literature are represented as solid lines with different shades of gray to distinguish them from each other[33,34,92–95]. In the inset, only the SESAME 83103 Ni Hugoniot is represented for clarity. Yellow star represents run 493, the highest pressure run we obtained with usable VISAR data and XRD data. For this run, note that pressure was measured with VISAR, whereas temperature was not measured. This point is the result of placing the pressure value onto the principal single-phase Hugoniot.

A recent study used X-ray absorption spectroscopy (XAS) to examine statically compressed and laser-heated samples of Ni, yielding a wide range of both solid and liquid data against which to compare the various melt studies[70,79]. Although these data tend to support the more recent predictions of a steeper melt line, the XAS data were measured only up to ~100 GPa, limiting the ability to constrain the melt line under much higher pressures using these data. Figure 3 shows a comparison of all Ni melting studies along with several Hugoniot models, including multi-phase and single-phase computational studies[33,34,92–95]. At pressures below 100 GPa, the Hugoniot lies well below the seven computational melt lines of varying slope that have been proposed in the literature. At pressures between 100 GPa and 300 GPa, the variation in the slope of proposed melt lines is large (Fig. 3, main panel), leading to intercepts with the Hugoniot ranging from as low as ~170 GPa to as high as ~290 GPa.

The peak pressures reached in each of the seven runs reported here from experiment LV13 range from (183 ± 23) GPa to (527 ± 87) GPa, which covers the broad range of intercepts expected across all of the reported melt lines in the literature. For the three lowest pressure runs (183 ± 23 GPa, 240 ± 18 GPa, 377 ± 38 GPa) we see no evidence of melt, suggesting that the onset of melt occurs at higher pressures along the Hugoniot. In the next three higher-pressure runs (486 ± 35 GPa, 515 ± 67 GPa, and 531 ± 52 GPa), evidence of melted nickel is present, suggesting that the onset of melt occurs below 486 ± 35 GPa. Thus, we are able to bracket the onset of melt between 377 ± 38 GPa and 486 ± 52 GPa. This range is significantly higher than the vast majority of literature melt lines. The appearance of full melt in the highest pressure run 149 (527 ± 87 GPa) suggests an upper pressure for melt completion at ~500 GPa.

The observation of fcc-Ni up to 531 ± 52 GPa implies a coexistence of melt over a pressure range of at least ~45 GPa, and perhaps even greater. This may be partly due to small differences in how much of the sample was compressed at the time of the X-ray probe, and thus could be influenced by the timescale of melting. We also note that our diagnostic has a minimum melt detectability that may influence our first observation of melt and the resulting inference of the coexistence region. Both of these points are discussed further in the Supporting Information.

In the L10075 experiment, we were able to collect VISAR data up to 332 ± 30 GPa, where we observed the solid compressed fcc phase of Ni at a density of 13.97 ± 0.07 g cm^{-3}. From the LV13 dataset, we can bracket the onset of melting to be in the region of 377 ± 38 GPa to 486 ± 35 GPa. If our higher pressure runs were also on-Hugoniot, then fcc-Ni may persist up to pressures as high as 531 ± 52 GPa.

We have reported in situ X-ray diffraction data measured up to pressures of ~500 GPa in shocked bulk nickel, which is the highest pressure reported to date for any structural study on this element. We observe the persistence of solid fcc-Ni on the principal Hugoniot up to at least 332 ± 30 GPa. Given that this measured incipient melting pressure is significantly higher than would be expected based on the majority of theoretical work, our results provide experimental support for a steeper melt line for nickel than for iron. The appearance of diffuse scattering at q-values consistent with dense liquid nickel indicates partial melting onset between 377 ± 38 GPa and 486 ± 35 GPa.

Our results place the nickel melt line above that of iron, which was also measured by X-ray diffraction at the National Ignition

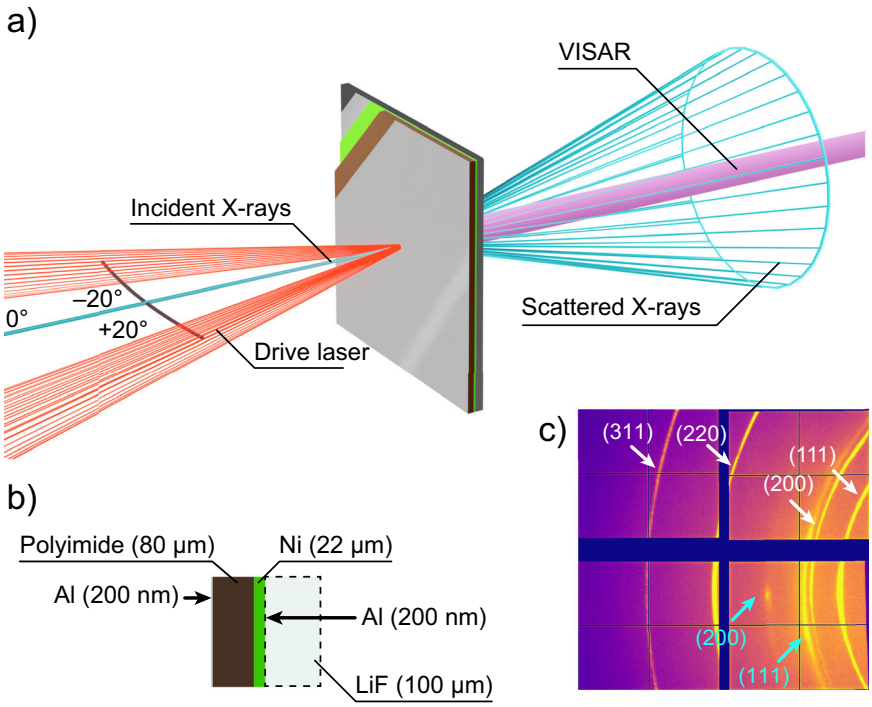

Fig. 4 | Overview of the experimental configuration and representative X-ray diffraction data. a Schematic representation of the experimental setup used to collect the VISAR and in situ X-ray diffraction data at the MEC hutch. The incident X-rays are normal to the sample plane, defined as 0°. The two drive lasers are focused onto the X-ray probe region, but each offset by ±20° in the horizontal plane. VISAR was performed at the Al–LiF interface. **b** The target package layer thicknesses for LV13. **c** Representative X-ray diffraction image from one of the four ePix 10k detectors is shown. Signals from the face-centered cubic (fcc) phase of Ni are highlighted. Reflections annotated in white indicate those of ambient nickel, while those annotated in teal indicate those of the compressed phase.

Facility and Dynamic Compression Sector[11,61]. Of particular note is the relative comparison between iron and nickel using a laser-shock compression platform and X-ray diffraction as the diagnostic of melting. Although temperature is not measured directly in these shock compression experiments, we can infer from the similarity between Fe and Ni thermoelasticity and Hugoniot relations that the melting of nickel occurs at significantly higher temperatures than iron at the conditions of the inner core boundary. In other words, the large difference in the onset of melting pressure can only be explained by a different shape of the melting curve, rather than by a higher temperature of Ni at the same Hugoniot state. Our melting inference for nickel is in contrast to previous work, in which static compression EXAFS data were used to place the nickel melt below that of iron[49]. On the other hand, the higher melting temperature of nickel is in agreement with recent computational work that found the nickel melt line to fall above the iron melt line at inner core conditions by ~700 K–800 K[35].

A steeper nickel melt line has implications for the chemistry and dynamics of Earth's inner core. Nickel has generally been assumed to mix nearly ideally with iron at inner core conditions based on much lower pressure measurements[31]. In a qualitative sense, the significantly higher melting temperature and fcc crystal structure at the inner core pressures imply that non-ideal contributions to the free energy of mixing could be present in the Fe–Ni system. This implies that the liquidus field of iron alloys that include nickel is broad and may promote an extended region of solid and liquid mixing at the inner core boundary[96]. Further investigation of nickel-bearing iron alloys may help inform dynamic models of inner core boundary "sediments" and the inclusion of extensive melt along grain boundaries within the inner core[9,97]. More generally, our results show that further research into the interaction between nickel and iron at core pressures is needed to determine the effect of alloying on the melting temperature.

Methods

Shock compression experiments were performed at the Matter in Extreme Conditions (MEC) endstation of the Linac Coherent Light Source (LCLS) at the SLAC National Accelerator Laboratory[98]. The data presented in this study were collected at MEC in the standard configuration during two separate campaigns (LV13 and L10075) with slightly different specifications. Experiments for the LV13 dataset were performed in the standard configuration, which is illustrated in Fig. 4. An ablatively-driven shockwave was launched into target packages using a 10 ns or 15 ns near flat-top pulse from four arms of a ~60 J laser ($\lambda = 527$ nm). The flat-top pulse shape shown in Supplementary Materials was selected in order to deliver a temporally steady shock to the material and yield a state upon the principal Hugoniot of nickel. The lasers had a nominal spot diameter of 150 μm, with 50% of the energy delivered over 140 μm. In some of the runs, 300 μm phase plates were used, with 50% of the energy delivered over 241 μm. The angles of incidence of the lasers were ±20° to the sample normal. The X-rays were directed normal to the sample, as shown in Fig. 4. Diffraction data was collected on four ePix 10k QUADS detectors (see IV B for details.)

The in-sample stress was varied through the rotation of a half-waveplate combined with a polarizer—both placed within the beam path—to attenuate the drive laser energy reaching the target. In all experiments except runs 420 and 422, a ~80 μm polyimide (Kapton-B) layer was used as the ablator; for runs 420 and 422, which had no window (free surface), we used a 100 μm polyimide layer. The polyimide layers were coated with 200 nm of aluminum on the laser drive side, and bonded to the sample with a thin layer of epoxy on the other side. The sample layer was 22 ± 3 μm-thick cold-rolled light-tested nickel foil purchased from Goodfellow. It was characterized as a fcc ($Fm\bar{3}m$) with $a = 3.5238$ Å ($\rho = 8.911\,\mathrm{g\,cm^{-3}}$). Windows consisted of ~100 μm-thick single crystals of (100)-LiF (lithium fluoride) that had been coated with 200 nm of Al. The Al-coated side of the windows was

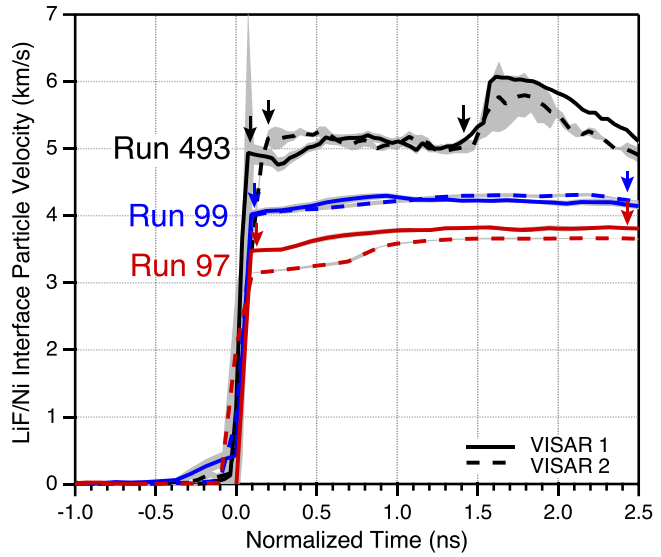

Fig. 5 | Velocity of the Ni/LiF interface versus time traces for run 097 (LV13, red), run 099 (LV13, blue), and run 493 (L10075, black). Solid traces represent data from VISAR 1, and dashed traces represent data from VISAR 2. Shaded regions reflect the standard deviation of the calculated particle velocity. Time is normalized to arrival at the Ni/LiF interface. Here, the transmitted compression waves are described by a fast initial rise, after which there is a distribution of velocity states up to a peak value. At late times, the velocity drops off due to a stress release associated with the end of the applied laser drive. Temporal unsteadiness in the peak compression state is attributed to non-ideal laser pulse shaping, reverberations within the epoxy glue layers of the sample, and, at late times, a reverberation within the Ni foil itself (this is visible 1.5 ns after breakout in run 493). Note that expected transit times of the shock through the Ni foil for each run are presented in Table 1, and range from 2.90 ns for run 097 to 1.16 ns for run 493. Determination of the average shock stress and distribution of stress states includes the range of velocity states above the initial shock. Error is shown as the shaded region surrounding each trace. Arrows indicate the region over which the range of velocities was considered, taking into account the transit times listed in Table 1 for each run.

bonded to the Ni foil with a thin layer of epoxy. The Al coating provided a reflective layer for velocity interferometry system for any reflector (VISAR) measurements[99].

Data from experiment L10075 was collected at MEC at a later date, but with a similar experimental setup. The most salient difference between L10075 and LV13 was the sample package design, and the differences are noted here. In L10075, the 50 μm polyimide ablator was coated with a 0.2 μm layer of platinum. The nickel foil was 12.5 μm, and the window was 100 μm of lithium fluoride with 0.3 μm of titanium as the reflective layer for VISAR measurements. In L10075, the optical drive laser had been upgraded to deliver a maximum of ~100 J of laser energy on target.

Pressure determination

Particle velocities were measured at the Ni–LiF interface using VISAR, wherein an Nd:YAG 532 nm laser light source was focused onto the Ni–LiF interface. We used line VISAR to collect spatial information along one dimension of the sample with a total field of view of 360 μm. Care was taken to ensure that this field of view overlapped with the X-ray focal spot (40 μm for LV13 and 20 μm for L10075) so that the measured velocities would be pertinent to the measured diffraction. Two VISAR channels were employed, with different velocity per fringe sensitivities, to resolve any potential fringe shift (velocity) ambiguity related to the U_P measurement of the near-instantaneous shock front[99]. For each reported run, the shock arrival time at the Ni–LiF interface is constant, within the temporal and spatial resolution of the VISAR streak camera, over the region probed by the X-rays.

The line-VISAR images from both VISAR streak cameras (VISAR 1 and VISAR 2) were analyzed to yield one-dimensional profiles of Ni–LiF interface velocity. These profiles are shown in Fig. 5. The uniformity of the velocity states after shock breakout captured by VISAR at the Ni–LiF interface indicated that the sample experienced a near-temporally steady shock. The timing of the sharp rise in the particle velocity gives a measure of the shock breakout time, while the mean of the peak velocities immediately following breakout gives a measure of the stress state achieved in the sample. The sample stresses were determined using impedance matching. Specifically, we used the linear fits for the dependence of U_S (shock velocity) on u_p (particle velocity) derived from the literature data on the equation of state of LiF[100] and literature data on the equation of state of Ni (Equations (1) and (2))[36–38,41–44,65,101].

$$U_{S,\mathrm{LiF}} = 5.1812(\pm 0.048) + 1.3065(\pm 0.025)u_{p,\mathrm{LiF}} \quad (1)$$

$$U_{S,\mathrm{Ni}} = 4.7239(\pm 0.048) + 1.1964(\pm 0.025)u_{p,\mathrm{Ni}} \quad (2)$$

Corrections were applied to account for the refractive index of LiF under shock compression[102].

The HYADES package was used to simulate the progression of the shockwave through the sample, allowing for an estimate of the pressure within each layer as well as the speed at which the shockwave traveled through the target package[103]. The results of these simulations are shown in the Supplementary Materials.

In our experiments, the sample is uniaxially compressed. While the use of the term "pressure" throughout the paper suggests a hydrostatically compressed state, we cannot rule out the presence of deviatoric stresses, which would—in the case of our measurements and indeed all previous Hugoniot measurements—give rise to higher values of longitudinal stress (as determined from our VISAR measurements) and therefore the reported pressure[33,34,92–95]. In the analysis of Fowles[104] using the Lévy–von Mises yield criterion[105], this stress deviation corresponds to two-thirds of the yield strength. However, while the high-pressure strength of Ni is unknown, strength measurements on other metals[106] suggest that the difference between the longitudinal stress and hydrostatic pressure in our experiments is on the order of a few GPa. This represents a systematic uncertainty in our reported pressure values.

In total, eight runs were taken over a range of shock pressures. Three of these runs (097, 099, and 493) used VISAR impedance matching analysis to determine the Ni sample pressures (183(23), 240(18), and 332(30) GPa). For other runs, where VISAR was not available due to poor target reflectivity, the sample pressure was constrained by a combination of hydrodynamic simulations, and laser intensity calibrations (see Supplementary Materials).

The laser intensity calibration curve uses the pressure values determined from a pressure–density relationship that we constructed using an equation of the form proposed by Drake and Lindl[107–109]. The fit is shown in the Supplementary Materials and the equation is given below (Equation (3)).

$$P_{\mathrm{Nickel}}[GPa] = 4215(\pm 1020)\left(\frac{I\left[\frac{PW}{cm^2}\right]}{0.527\mu\mathrm{m}}\right)^{0.662(\pm 0.070)} \quad (3)$$

This calibration curve is fitted to data with a maximum laser intensity of 2.22×10^{13} W cm^{-2} (2.22×10^{-2} PW cm^{-2}).

The uncertainty in stress is a contribution of the following: (i) the standard distribution of velocity states above the initial shock; (ii) the accuracy which fringe shifts can be measured[110] in the line-VISAR systems, taken here as 0.177 km s^{-1} for VISAR 1 and 0.039 km s^{-1} for VISAR 2 for the LV13 experiment (5% of a fringe shift; for the L10075

experiment, these values are 0.102 km s^{-1} for VISAR 1 and 0.242 km s^{-1} for VISAR 2) (iii) uncertainty in the LiF and Ni Hugoniot models; and (iv) for line-VISAR additional velocity uncertainties from spatial non-planarities in the compression drive[111] and random frequency structure on fringes which can shift the central position of a fringe (due to random intensity speckle structure emerging from the VISAR input fiber)[112]. Other contributors to stress uncertainty which are considered small relate to uncertainties in the refractive index of LiF[102], uncertainties in the timing of the X-ray probe with respect to the VISAR, uncertainties in the measurements of sample thickness, and non-uniformities in target layer thicknesses resulting in compression wave arrival at different times across the VISAR field of view.

X-ray diffraction

XRD data were collected in transmission geometry, with the incoming X-ray free-electron laser X-ray beam incident at 0° degrees to the sample normal. For the LV13 campaign, the self-amplified spontaneous emission–mode X-rays had a peak flux energy of 12.6 keV ($\lambda = 0.984$ Å). The X-rays were quasimonochromatic (0.2% $\Delta E/E$) and contained 10^{12} photons. Diffraction images were collected using four ePix 10k QUAD detectors arranged to capture diffraction over $q = 1.5$ $Å^{-1}$ to 7.5 $Å^{-1}$ ($q = 4\pi sin(\theta)/\lambda$, where λ is the X-ray wavelength and θ is the Bragg scattering angle). The pixel size of the ePix 10k QUADS is 100 µm by 100 µm. All of the XRD data reported in this work were collected with 50 fs duration X-ray pulses with an on-sample 40 µm spot diameter.

The data for the L10075 experiment (run 493) was collected using X-rays with a peak flux energy of 10.1 keV ($\lambda = 1.23$ Å), and with an on-sample spot diameter of 20 µm. This experiment also used the ePix 10k QUAD detectors, but Q2 was positioned differently to capture high-angle data. Raw X-ray diffraction images are shown in the Supplementary Materials. Processed diffractograms are shown in Fig. 1. A detailed discussion on the calibration procedure and handling of the X-ray diffraction is present in the Supporting Materials.

In all reported data, the X-rays probed the sample before shock breakout at the Ni–LiF interface, ensuring that only peak pressure states and ambient (unshocked) sample were measured. XRD data were recorded on each sample prior to laser-shock experiments, and then in situ data were collected during laser-shock compression.

Data availability

The raw X-ray diffraction and VISAR images used in this study are available in the Figshare database using the following link [https://doi.org/10.6084/m9.figshare.28477868].

Code availability

The data analysis code implementing the methods described in the Supplementary Materials is available at https://github.com/ScottNotFound/pymeccano.

References

1. McDonough, W. F. & Sun, S. S. The composition of the earth. *Chem. Geol.* **120**, 223–253 (1995).
2. Sossi, P. A. A nickel for your planet's thoughts. *Nat. Geosci.* **10**, 249–251 (2017).
3. McDonough, W. F. Compositional model for the earth's core. *Treatise Geochem.* **2-9**, 547–568 (2003).
4. Hirose, K., Labrosse, S. & Hernlund, J. Composition and state of the core. *Annu. Rev. Earth Planet. Sci.* **41**, 657–691 (2013).
5. Hausoel, A. et al. Local magnetic moments in iron and nickel at ambient and earth's core conditions. *Nat. Commun.* **8**, 16062 (2017).
6. Lehmann, I. *P' As Read From The Records Of The Earthquake of June 16th, 1929* (Akademische Verlagsgesellschaft, 1930). https://cir.nii.ac.jp/crid/1130000796162622720.bib?lang=en.
7. Pham, T. S. & Tkalčić, H. Up-to-fivefold reverberating waves through the earth's center and distinctly anisotropic innermost inner core. *Nat. Commun.* **14**, 754 (2023).
8. Pang, G. et al. Enhanced inner core fine-scale heterogeneity towards earth's centre. *Nature* **620**, 570–575 (2023).
9. Singh, S. C., Taylor, M. A. & Montagner, J. P. On the presence of liquid in earth's inner core. *Science* **287**, 2471 (2000).
10. Prescher, C. et al. High poisson's ratio of earth's inner core explained by carbon alloying. *Nat. Geosci.* **8**, 220–223 (2015).
11. Kraus, R. G. et al. Measuring the melting curve of iron at super-earth core conditions. *Science* **375**, 202–205 (2022).
12. Anzellini, S., Dewaele, A., Mezouar, M., Loubeyre, P. & Morard, G. Melting of iron at earth's inner core boundary based on fast x-ray diffraction. *Science* **340**, 464–466 (2013).
13. Boehler, R., Bargen, N. V. & Chopelas, A. Melting, thermal expansion, and phase transitions of iron at high pressures. *J. Geophys. Res.* **95**, 21731–21736 (1990).
14. Boehler, R. Temperatures in the earth's core from melting-point measurements of iron at high static pressures. *Nature* **363**, 534–536 (1993).
15. Sinmyo, R., Hirose, K. & Ohishi, Y. Melting curve of iron to 290 GPa determined in a resistance-heated diamond-anvil cell. *Earth Planet. Sci. Lett.* **510**, 45–52 (2019).
16. Konôpková, Z. et al. Laser heating system at the extreme conditions beamline, p02.2, petra iii. *J. Synchrotron Radiat.* **28**, 1747–1757 (2021).
17. Morard, G. et al. Solving controversies on the iron phase diagram under high pressure. *Geophys. Res. Lett.* **45**, 11074–11082 (2018).
18. Jackson, J. M. et al. Melting of compressed iron by monitoring atomic dynamics. *Earth Planet. Sci. Lett.* **362**, 143–150 (2013).
19. Alfè, D. Temperature of the inner-core boundary of the earth: melting of iron at high pressure from first-principles coexistence simulations. *Phys. Rev. B* **79**, 060101 (2009).
20. Swift, D. C., Lockard, T., Smith, R. F., Wu, C. J. & Benedict, L. X. High pressure melt curve of iron from atom-in-jellium calculations. *Phys. Rev. Res.* **2**, 023034 (2020).
21. Belonoshko, A. B., Ahuja, R. & Johansson, B. Quasi-ab initio molecular dynamic study of fe melting. *Phys. Rev. Lett.* **84**, 3638–3641 (2000).
22. Wu, Y. N., Wang, D. M. & Huang, Y. S. Melting of iron at the earths core conditions by molecular dynamics simulation. *AIP Adv.* **1**, 032122 (2011).
23. Wu, C. J. et al. Wide-ranged multiphase equation of state for iron and model variations addressing uncertainties in high-pressure melting. *Phys. Rev. B* **108**, 014102 (2023).
24. Sjostrom, T. & Crockett, S. Quantum molecular dynamics of warm dense iron and a five-phase equation of state. *Phys. Rev. E* **97**, 053209 (2018).
25. Benedict, L. X., Kraus, R. G., Hamel, S. & Belof, J. L. *A Limited-ranged Two-phase Iron Equation Of State Model*. Tech. Rep., Lawrence Livermore National Laboratory https://www.osti.gov/biblio/1843135 (2022).
26. Nguyen, J. H. & Holmes, N. C. Melting of iron at the physical conditions of the earth's core. *Nature* **427**, 339–342 (2004).
27. Brown, J. M. & McQueen, G. Phase transitions, grüneisen parameter, and elasticity for shocked iron between 77 GPa and 400 GPa. *J. Geophys. Res.* **91**, 7485–7494 (1986).
28. Yoo, C. S., Holmes, N. C., Ross, M., Webb, D. J. & Pike, C. Shock temperatures and melting of iron at earth core conditions. *Phys. Rev. Lett.* **70**, 3931–3934 (1993).
29. Turneaure, S. J., Sharma, S. M. & Gupta, Y. M. Crystal structure and melting of Fe shock compressed to 273 GPa: in situ x-ray diffraction. *Phys. Rev. Lett.* **125**, 215702 (2020).

30. Komabayashi, T. Thermodynamics of the system fe-si-o under high pressure and temperature and its implications for earth's core. *Phys. Chem. Miner.* **47**, 387 (2020).
31. Mao, W. L., Campbell, A. J., Heinz, D. L. & Shen, G. Phase relations of fe-ni alloys at high pressure and temperature. *Phys. Earth Planet. Inter.* **155**, 146–151 (2006).
32. Komabayashi, T. et al. Phase relations in the system fe-ni-si to 200 GPa and 3900 k and implications for earth's core. *Earth Planet. Sci. Lett.* **512**, 83–88 (2019).
33. Belashchenko, D. K. Computer simulation of nickel and the account for electron contributions in the molecular dynamics method. *High. Temp.* **58**, 64–77 (2020).
34. Smirnov, N. A. Ab initio calculations of structural stability, thermodynamic and elastic properties of ni, pd, rh, and ir at high pressures. *J. Appl. Phys.* **134**, 025901 (2023).
35. Sun, Y. et al. Unveiling the effect of Ni on the formation and structure of earth's inner core. *Proceed. Natl. Acad. Sci. USA* **121**, e2316477121 (2024).
36. Walsh, J. M., Rice, M. H., Mcqueen, R. G. & Yarger, F. L. Shock-wave compressions of twenty-seven metals. equations of state of metals*. *Phys. Rev.* **108**, 195–216 (1957).
37. McQueen, R. G. & Marsh, S. P. Equation of state for nineteen metallic elements from shock-wave measurements to two megabars. *J. Appl. Phys.* **31**, 1253–1269 (1960).
38. Kormer, S. B., Funtikov, A. I., Urlin, V. D. & Kolesnikova, A. N. Dynamic compression of porous metals and the equation of state with variable specific heat at high temperatures. *J. Exptl. Theor. Phys.* **15**, 686–702 (1962).
39. Al'tshuler, L. V. et al. Shock adiabatic curves of metals. new data, statistical analysis, and general laws. *Zh. Eksp. Teor. Fiz.* **42**, 91–104 (1962).
40. Urlin, V. D. Melting at ultra high pressures in a shockwave. *J. Exptl. Theor. Phys.* **22**, 485–492 (1966).
41. Isbell, W., Shipman, F. & Jones, A. *Hugoniot Equation Of State For Eleven Materials To Five Megabars*. Tech. Rep., General Motors Corporation (1968).
42. Marsh, S.P. *LASL shock Hugoniot data* (University of California Press, Berkeley, CA, 1980).
43. Al'tshuler, L. V. et al. Shock adiabatic curves of metals. *J. Appl. Mech. Tech. Phys.* **22**, 145–169 (1981).
44. Trunin, R. F. et al. Compressibility of porous metals in shock waves. *Phys. JETP* **69**, 580 (1989).
45. Dolgoborodov, A. Y. et al. Shock hugoniot of porous nanosized nickel. *J. Appl. Phys.* **131**, 125902 (2022).
46. Lythgoe, K. H., Deuss, A., Rudge, J. F. & Neufeld, J. A. Earth's inner core: innermost inner core or hemispherical variations? *Earth Planet. Sci. Lett.* **385**, 181–189 (2014).
47. Wang, S. & Tkalčić, H. Shear-wave anisotropy in the earth's inner core. *Geophys. Res. Lett.* **48**, e2021GL094784 (2021).
48. Polsin, D. N. et al. Atomic structure and melting of ni and $fe_{36}Ni$ up to 400 GPa. *Phys. Rev. B* **109**, 214112 (2024).
49. Torchio, R. et al. Melting curve and phase relations of fe-ni alloys: Implications for the earth's core composition. *Geophys. Res. Lett.* **47**, 1–7 (2020).
50. Minakov, D. V. & Levashov, P. R. Melting curves of metals with excited electrons in the quasiharmonic approximation. *Phys. Rev. B* **92**, 224102 (2015).
51. Wark, J. S., McMahon, M. I. & Eggert, J. H. Femtosecond diffraction and dynamic high pressure science. *J. Appl. Phys.* **132** https://pubs.aip.org/aip/jap/article/132/8/080902/2837271/Femtosecond-diffraction-and-dynamic-high-pressure (2022).
52. Duffy, T. S. & Smith, R. F. Ultra-high pressure dynamic compression of geological materials. *Front. Earth Sci.* **7**, 1–20 (2019).
53. Hamilton, B. W., Sakano, M. N., Li, C. & Strachan, A. Chemistry under shock conditions. *Annu. Rev. Mater. Res.* **51**, 1–20 (2021).
54. Ichiyanagi, K. & Nakamura, K. G. Structural dynamics of materials under shock compression investigated with synchrotron radiation. *Metals* **6**, 17 (2016).
55. McMahon, M. I. High-pressure crystallography. *Top. Curr. Chem.* **315**, 69–110 (2012).
56. Mao, H. K. et al. Recent advances in high-pressure science and technology. *Matter Radiat. Extremes* **1**, 59–75 (2016).
57. Pascarelli, S. et al. Materials under extreme conditions using large x-ray facilities. *Nat. Rev. Methods Prim.* **3**, 82 (2023).
58. Cerantola, V. et al. New frontiers in extreme conditions science at synchrotrons and free electron lasers. *J. Phys. Condens. Matter* **33**, 274003 (2021).
59. Wang, J. et al. X-ray diffraction of molybdenum under shock compression to 450 GPa. *Phys. Rev. B.* **92**, 1–9 (2015).
60. Kraus, R. G. et al. Melting of tantalum at multimegabar pressures on the nanosecond timescale. *Phys. Rev. Lett.* **126**, 255701 (2021).
61. Singh, S. et al. Structural study of hcp and liquid iron under shock compression up to 275 GPa. *Phys. Rev. B* **108**, 184104 (2023).
62. Davis, P. et al. X-ray scattering measurements of dissociation-induced metallization of dynamically compressed deuterium. *Nat. Commun.* **7**, 1–8 (2016).
63. Hawreliak, J. A., Winey, J. M., Toyoda, Y., Wallace, M. & Gupta, Y. M. Shock-induced melting of [100] lithium fluoride: sound speed and hugoniot measurements to 230 GPa. *Phys. Rev. B* **107**, 014104 (2023).
64. Kerley, G. I. Calculation of release adiabats and shock impedance matching. Preprint at *arxiv* https://arxiv.org/abs/1306.6913 (2013).
65. Al'tshuler, L. V., Bakanova, A. A. & Trunin, R. F. Shock adiabats and zero isotherms of seven metals at high pressures. *J. Exptl. Theor. Phys.* **15**, 91–104 (1962).
66. Toby, B. H. & Dreele, R. B. V. GSAS-II: The genesis of a modern open-source all purpose crystallography software package. *J. Appl. Crystallogr.* **46**, 544–549 (2013).
67. Errandonea, D. High-pressure melting curves of the transition metals Cu, Ni, Pd, and Pt. *Phys. Rev. B* **87**, 054108 (2013).
68. Lazor, P., Shen, G. & Saxena, S. K. Physics chemisiry minerals laser-heated diamond anvil cell experiments at high pressure: melting curve of nickel up to 700 kbar. *Phys. Chem. Miner.* **20**, 86–90 (1993).
69. Aquilanti, G. et al. Melting of iron determined by x-ray absorption spectroscopy to 100 GPa. *Proc. Natl Acad. Sci. USA* **112**, 12042–12045 (2015).
70. Boccato, S. et al. The melting curve of nickel up to 100 GPa explored by XAS. *J. Geophys. Res. Solid Earth* **122**, 9921–9930 (2017).
71. Anzellini, S. et al. In situ characterization of the high pressure - high temperature melting curve of platinum. *Sci. Rep.* **9**, 13034 (2019).
72. Salamat, A., Fischer, R. A., Briggs, R., McMahon, M. I. & Petitgirard, S. In situ synchrotron x-ray diffraction in the laser-heated diamond anvil cell: melting phenomena and synthesis of new materials. *Coord. Chem. Rev.* **277**, 15–30 (2014).
73. Saha, P. & Mukherjee, G. D. Thermal conductivity of iron and nickel during melting: implication to the planetary liquid outer core. *Pramana* **97**, 1 (2023).
74. Gorman, M. G. et al. Direct observation of melting in shock-compressed bismuth with femtosecond x-ray diffraction. *Phys. Rev. Lett.* **115**, 1–5 (2015).
75. Briggs, R. et al. High-pressure melting behavior of tin up to 105 GPa. *Phys. Rev. B* **95**, 054102 (2017).
76. Briggs, R. et al. Coordination changes in liquid tin under shock compression determined using in situ femtosecond x-ray diffraction. *Appl. Phys. Lett.* **115**, 264101 (2019).

77. Page, D. I. & March, N. H. Neutron scattering and atomic dynamics in liquid nickel. *Phys. Chem. Liq.* **6**, 243–260 (1977).
78. Edert, J. et al. The structure factor of liquid nickel at 1873 K. *J. Phys. F: Met. Phys.* **9**, 1215 (1979).
79. Boccato, S. et al. Compression of liquid Ni and Co under extreme conditions explored by x-ray absorption spectroscopy. *Phys. Rev. B* **63**, 220401 (2019).
80. Luo, F., Chen, X. R., Cai, L. C. & Ji, G. F. Solid-liquid interfacial energy and melting properties of nickel under pressure from molecular dynamics. *J. Chem. Eng. Data* **55**, 5149–5155 (2010).
81. Zhang, W. J., Liu, Z. L. & Peng, Y. F. Molecular dynamics simulations of the melting curves and nucleation of nickel under pressure. *Phys. B: Condens. Matter* **449**, 144–149 (2014).
82. Lord, O. T. et al. The melting curve of Ni to 1 Mbar. *Earth Planet. Sci. Lett.* **408**, 226–236 (2014).
83. Errandonea, D. et al. Systematics of transition-metal melting. *Phys. Rev. B.* **63**, 220401 (2001).
84. Japel, S., Schwager, B., Boehler, R. & Ross, M. Melting of copper and nickel at high pressure: the role of d electrons. *Phys. Rev. Lett.* **95**, 167801 (2005).
85. Cao, Q. L. et al. Properties of liquid nickel along melting lines under high pressure. *Chin. Phys. Lett.* **32**, 116–119 (2015)
86. Pozzo, M. & Alfè, D. Melting curve of face-centered-cubic nickel from first-principles calculations. *Phys. Rev. B* **88**, 024111 (2013).
87. Koči, L. et al. Simulation of shock-induced melting of Ni using molecular dynamics coupled to a two-temperature model. *Phys. Rev. B* **74**, 012101 (2006).
88. Hieu, H. K. Systematic prediction of high-pressure melting curves of transition metals. *J. Appl. Phys.* **116**, 163505 (2014).
89. Ross, M., Boehler, R. & Errandonea, D. Melting of transition metals at high pressure and the influence of liquid frustration: the late metals Cu, Ni, and Fe. *Phys. Rev. B* **76**, 184118 (2007).
90. Hoc, N. Q., Cuong, T. D., Tinh, B. D. & Viet, L. H. High-pressure melting curves of fcc metals Ni, Pd and Pt with defects. *Mod. Phys. Lett. B* **33**, 1950300 (2019).
91. Zhao, L., Hamel, S., Lordi, V. & Samanta, A. High pressure melt line of nickel using a generalized embedded atomic method potential. *Appl. Phys. Lett.* **124**, 234102 (2024).
92. Lyon, S. & Johnson, J. SESAME: *The Los Alamos National Laboratory Equation Of State Database.* Report No. LA-UR-92-3407. Tech. Rep., Los Alamos National Laboratory (1992).
93. Sjostrom, T. *Sesame Equation of State for Nickel.* Report No. LA-UR-22-21063. Tech. Rep., Los Alamos National Laboratory (2022).
94. Prisbrey, C. J., Soderlind, P. & Wu, C. J. *A New Multiphase Equation Of State Table For Ni*. Report No. Llnl-proc-856971. Tech. Rep., Lawrence Livermore National Laboratory (2023).
95. Kerley, G. I. *Equations Of State For Be, Ni, W, And Au.* Report no. sand-2003-3784. Tech. Rep., Sandia National Laboratories https://www.osti.gov/biblio/918304 (2003).
96. Zhang, Y., Nelson, P., Dygert, N. & Lin, J. F. Fe alloy slurry and a compacting cumulate pile across earth's inner-core boundary. *J. Geophys. Res. Solid Earth* **124**, 10954–10967 (2019).
97. Buffett, B. A., Garnero, E. J. & Jeanloz, R. Sediments at the top of earth's core. *Science* **290**, 1338–1342 (2000).
98. Nagler, B. et al. The matter in extreme conditions instrument at the linac coherent light source. *J. Synchrotron Radiat.* **22**, 520–525 (2015).
99. Celliers, P. M. et al. Line-imaging velocimeter for shock diagnostics at the omega laser facility. *Rev. Sci. Instrum.* **75**, 4916–4929 (2004).
100. Davis, J.-P., Knudson, M. D., Shulenburger, L. & Crockett, S. D. Mechanical and optical response of [100] lithium fluoride to multi-megabar dynamic pressures. *J. Appl. Phys.* **120**, 165901 (2016).
101. Hirao, N., Akahama, Y. & Ohishi, Y. Equations of state of iron and nickel to the pressure at the center of the earth. *Matter Radiat. Extremes* **7**, 038403 (2022).
102. Rigg, P. A., Knudson, M. D., Scharff, R. J. & Hixson, R. S. Determining the refractive index of shocked [100] lithium fluoride to the limit of transmissibility. *J. Appl. Phys.* **116**, 033515 (2014).
103. Larsen, J. T. & Lane, S. M. Hyades-a plasma hydrodynamics code for dense plasma studies. *J. Quant. Spectrosc. Radiat. Transf.* **51**, 179–186 (1994).
104. Fowles, G. R. Shock wave compression of hardened and annealed 2024 aluminum. *J. Appl. Phys.* **32**, 1475–1487 (1961).
105. Hill, R. *The mathematical theory of plasticity*. In Oxford Classic Texts in the Physical Sciences (Oxford University Press, 1998).
106. Krygier, A. et al. Extreme hardening of pb at high pressure and strain rate. *Phys. Rev. Lett.* **123**, 205701 (2019).
107. Brown, S. B. et al. Shock drive capabilities of a 30-Joule laser at the matter in extreme conditions hutch of the Linac coherent light source. *Rev. Sci. Instrum.* **88**, 105113 (2017).
108. Drake, R. P., Davison, L. & Horie, Y. *High-energy-density Physics: Fundamentals, Inertial Fusion, And Experimental Astrophysics* (Springer Berlin, Heidelberg, 2006).
109. Lindl, J. Development of the indirect-drive approach to inertial confinement fusion and the target physics basis for ignition and gain. *Phys. Plasmas* **2**, 3933–4024 (1995).
110. Dolan, D. *Foundations of visar analysis*. Tech. Rep., Sandia National Laboratories (SNL) https://www.osti.gov/servlets/purl/886901/ (2006).
111. Glenzer, S. H. et al. Matter under extreme conditions experiments at the Linac coherent light source. *J. Phys. B: At. Mol. Opt. Phys.* **49**, 092001 (2016).
112. Erskine, D. Speckle-adaptive visar fringe analysis technique. *AIP Conf. Proc.* **1793**, 160017 (2017).

Acknowledgements

We thank the staff at the MECs endstation of the Linac Coherent Light Source for their expertise in conducting these experiments. We thank Travis Volz at Lawrence Livermore National Laboratory for his assistance with this project. We thank Nathan Pulver at the University of California, Los Angeles, for his assistance with beamtime. We thank Scott Thiel for writing and assisting with the scripts used to work up the experimental data. Lawrence Livermore National Laboratory is operated by Lawrence Livermore National Security, LLC, for the US Department of Energy, National Nuclear Security Administration under Contract No. DE-AC52-07NA2734 and was supported by the LLNL-LDRD Program under Project Nos. 21-ERD-032. Document number: LLNL-JRNL-866398. Use of the LCLS, SLAC National Accelerator Laboratory, is supported by the U.S. Department of Energy, Office of Science, Office of Basic Energy Sciences under Contract No. DE-AC02-76SF00515. The MEC instrument is supported by the U.S. Department of Energy, Office of Science, Office of Fusion Energy Sciences under Contract No. SF00515.

Author contributions

S.M.C. and R.F.S. conceived the project. K.A.P., S.M.C., S.S., R.F.S., and J.P.S.W. designed the experiments. C.D. assembled the targets. K.A.P., S.M.C., S.S., R.B., C.P.M, D.M., C.V., M.G.G., A.L.C., and J.P.S.W. performed the experiments. H.J.L., D.K., B.N., E.G., and E.C. advised on the experimental setup and assisted in data collection at SLAC. S.J.T. contributed calibration data. T.H. and J.H.E. contributed code to the data analysis. K.A.P. analyzed the data with guidance from S.M.C., S.S., R.B., R.F.S., and J.P.S.W. M.G.G., D.M., C.P.M., and R.B. contributed to the interpretation of the data. K.A.P. and J.P.S.W. wrote the manuscript.

Competing interests

The authors declare no competing interests.

Additional information

Supplementary information The online version contains supplementary material available at https://doi.org/10.1038/s41467-025-59385-y.

Correspondence and requests for materials should be addressed to Samantha M. Clarke or James P. S. Walsh.

Peer review information *Nature Communications* thanks Prithachakaran Renganathan, Youjun Zhang and the other, anonymous, reviewer(s) for their contribution to the peer review of this work. A peer review file is available.